

# Galaxy-lens determination of $H_0$ : constraining density slope in the context of the mass sheet degeneracy

Matthew R. Gomer, Liliya L. R. Williams

*School of Physics and Astronomy, University of Minnesota, 116 Church Street SE, Minneapolis MN, 55455, USA*

Accepted XXX. Received YYY; in original form ZZZ

## ABSTRACT

Gravitational lensing offers a competitive method to measure  $H_0$  with the goal of 1% precision. A major obstacle comes in the form of lensing degeneracies, such as the mass sheet degeneracy (MSD), which make it possible for a family of density profiles to reproduce the same lensing observables but return different values of  $H_0$ . The modeling process artificially selects one choice from this family, potentially biasing the recovered value of  $H_0$ . The effect is more pronounced when the profile of a given lens is not perfectly described by the lens model, which will always be the case to some extent. To explore this, we quantify the bias and spread by creating quads from two-component mass models and fitting them with a power-law ellipse+shear model. We find that the bias does not correspond to the estimate one would calculate by transforming the profile into a power law near the image radius. We also emulate the effect of including stellar kinematics by performing fits where the slope is constrained to the true value over a range of radii. Constraining the slope to the true value near the image radius can introduce substantial bias (0–8% for our most realistic models). We conclude that lensing degeneracies manifest in a more complicated way than is assumed. If stellar kinematics incorrectly break the MSD, their inclusion may introduce more bias than their omission.

**Key words:** gravitational lensing: strong – distance scale – galaxies: haloes – galaxies: stellar content

## 1 INTRODUCTION

Robust determination of the Hubble constant is one of the most sought-after goals in cosmology. Over the years, increasingly precise measurements of temperature anisotropies in the cosmic microwave background (CMB) have recovered values of  $H_0$  with smaller and smaller uncertainties. At present, the most precise CMB constraints come from the Planck mission, which found  $H_0 = 67.36 \pm 0.54$  km s<sup>-1</sup>Mpc<sup>-1</sup> (0.7% uncertainty), assuming  $\Lambda$ CDM cosmology (Planck Collaboration et al. 2018). Baryon Acoustic Oscillation (BAO) results from the Dark Energy Survey are broadly consistent with CMB results (Abbott et al. 2018).

Meanwhile, standard candle observations using Type Ia supernovae and Cepheid variables provide a direct distance measurement to faraway galaxies, allowing  $H_0$  to be measured directly rather than recovered from a model with many parameters (Riess et al. 2016). The tradeoff is that this method is dependent on the calibration of these standard candles, where any uncertainties in local measurements propagate to farther measurements. This method has been able to compete with the precision of CMB observations and, through improvements in the calibration, has presently

determined value of  $H_0 = 74.03 \pm 1.42$  km s<sup>-1</sup>Mpc<sup>-1</sup> (1.91% uncertainty) (Riess et al. 2019).

Tension exists between these two methods at the  $4.4\sigma$  level. The cause of this tension is unknown at present. These two methods compare the directly-measured local value of  $H_0$  to the most distant possible determination at the time of recombination, meaning they probe the expansion of the universe from one end to another. It might turn out that the prevailing model is more complicated than  $\Lambda$ CDM, hinting at new physics beyond the standard model or general relativity, perhaps through time-dependent dark energy or some other mechanism (Riess et al. 2016). On the other hand, it might turn out that the uncertainties of these two methods are missing some source of systematic error, and are thus underestimated. If the Milky Way resides within a local void, the measured value of  $H_0$  will be systematically biased with respect to the true value, although at present it does not seem that this effect would be sufficient to resolve the tension (Fleury et al. 2017; D’Arcy Kenworthy et al. 2019). Perhaps the answer lies in the standard candle calibration—Freedman et al. (2019) recently found that replacing the Cepheid variable calibration with the Tip of the Red Giant

Branch (TRGB) distance indicator results in a lower value of  $H_0 = 69.8 \pm 0.8$  ( $\pm 1.1\%$  stat)  $\pm 1.7$  ( $\pm 2.4\%$  sys)  $\text{km s}^{-1}\text{Mpc}^{-1}$ , only  $1.2\sigma$  away from the CMB result. It might turn out to be random chance that the methods disagree and as more data is collected they may converge to the same value. To diagnose the existence of the tension between these methods, an additional independent method would be exceedingly useful.

Strong gravitational lensing offers this independent method. If a variable source is multiply imaged, the difference in arrival time between the images offers a measurement of the time delay distance,  $D_{\Delta t} = (1 + z_d) \frac{D_d D_s}{D_{ds}} \propto \frac{1}{H_0}$  (Refsdal 1964). If one has an accurate model of the lensing potential for the mass distribution of the lens, it is straightforward to measure  $H_0$  from such information (Schechter et al. 1997; Suyu et al. 2010, 2017). The challenge is to precisely determine the time delays and lensing potential. Improvements in the method over time have enabled constraints on  $H_0$  to be placed at the 7% level using a single system (Suyu et al. 2010, 2014). Further improvements can be gained by combining constraints using multiple systems to average over variations between individual lenses. The tightest constraints from this method come from the state-of-the-art H0LiCOW ( $H_0$  Lenses in COSMOGRAIL’s Wellspring) program (Suyu et al. 2017). H0LiCOW gets time delays from the COSMOGRAIL (COSmological MONitoring of GRAvitational Lenses) program (Courbin et al. 2004; Bonvin et al. 2016), which has been monitoring light curves of multiply imaged systems for 15 years to date, measuring time delays within 1-3% uncertainty (Rathna Kumar et al. 2013; Tewes et al. 2013). H0LiCOW models lenses using image positions, fluxes, and time delays, as well as stellar kinematics of the lens galaxy (Wong et al. 2017). The analysis incorporates a variety of effects, such as inclusion of nearby group members (Sluse et al. 2017) and an estimation of line-of-sight external convergence (Rusu et al. 2017). Most recently, a blind combined analysis of six systems yielded a measurement of  $H_0 = 73.3^{+1.7}_{-1.8}$   $\text{km s}^{-1}\text{Mpc}^{-1}$  (2.4% uncertainty) (Wong et al. 2019).

In order to provide insight into the nature of the  $H_0$  tension, the uncertainty in the method must be competitive with the existing methods. The ambitious goal of the community is to reduce the uncertainties of the time delay method to 1% (Suyu et al. 2017). Bonvin et al. (2017) outline four actions which must be taken in order to reach such high precision: 1. Enlarge the sample, 2. Improve the lens model accuracy, 3. Improve the mass calibration through spatially resolved kinematics, and 4. Increase the efficiency of time delay measurement techniques. While the other actions are certainly important, the focus of this paper will be on the second and third: improving the lens model accuracy and studying the role of kinematic information. As Bonvin et al. (2017) put it, “as the number of systems being analysed grows, random uncertainties in the cosmological parameters will fall, and residual systematic uncertainties related to degeneracies inherent to gravitational lensing will need to be investigated in more detail.” Put another way, the statistical scatter due to a small sample size will decrease with time, but any biases inherent to lens modeling will not go away, potentially offsetting the recovered value from the true value. It is crucial that all biases intrinsic to the modeling process are carefully accounted for.

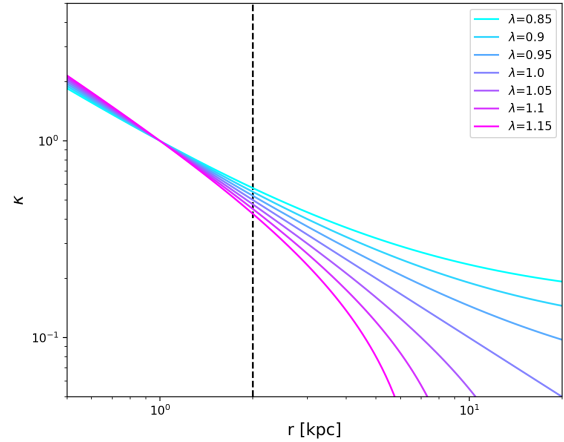


**Figure 1.** To illustrate the effect of the mass sheet degeneracy, an isothermal power-law profile is transformed by different values of  $\lambda$ . The Einstein radius for this example lies at 2.0 kpc (dashed line). The resulting slope near this radius is quite different for different values of  $\lambda$ . All of these profiles would be equally well supported by lensing information, but when fitting to a model profile shape, one of these solutions is preferentially selected.

### 1.1 Effect of lensing degeneracies

The source of the problem comes from lensing degeneracies, where the same observables can be recovered with multiple different lens models. There exist many types of degeneracies, the most famous of which is the exact mass sheet degeneracy (MSD) (Falco et al. 1985), where image positions and relative fluxes are left unchanged by a rescaling of the profile normalization and the corresponding introduction of a uniform convergence.

$$\kappa_\lambda(\vec{x}) = \lambda\kappa(\vec{x}) + (1 - \lambda) \quad (1)$$

Meanwhile,  $\lambda$  does affect the product of  $H_0$  and the time delay:  $H_0\Delta t \rightarrow \lambda H_0\Delta t$ , meaning that the recovered value of  $H_0$  will be biased by a factor of  $\lambda$ . For any lens model, the MSD allows for flexibility in the profile shape, since a range of profiles with varying  $\lambda$  would all reproduce the same observables. In principle, any of those profiles are equally supported by the data, but in practice, only one is chosen by the modeling process (Schneider & Sluse 2013). The effect of the MSD on a power-law shape is illustrated in Figure 1 for several values of  $\lambda$ . During modeling, the lens profile is assumed to follow a simple analytical shape, like a power law or a NFW profile. This forces  $\lambda$  to take on the particular value that makes the profile fit that shape in the region where images are located. In this way, a simplifying assumption could impose a value of  $\lambda$  (and therefore  $H_0$ ) which is not necessarily the same as the true mass distribution, as it has been artificially selected by the model choice.

It is worth emphasizing that this systematic effect is caused by lensing degeneracies inherent to all lens modeling and is not specific to any particular profile. Though this paper will be specifically exploring the effects with respect to a power-law model, any other profile would also be biased toward the particular value of  $\lambda$  which causes the mass distribution to most closely match the assumed profile. Even

sophisticated methods which use a Bayesian framework to determine the most likely of multiple different models (such as Autolens, [Nightingale et al. \(2018\)](#)) will be subject to systematic effects of degeneracies, although the nature of the systematic effects will likely be correspondingly more intricate. The exploration of these effects must start with simpler lens models.

The combined effect of the MSD and simplifying assumptions about the density profile shape has recently been analyzed by [Xu et al. \(2016\)](#). The authors extracted galaxies from the Illustris simulation along different lines of sight and looked at their lens profiles. They calculated the  $\lambda$  necessary to transform each profile into a straight power-law shape (with slope  $s_\lambda$ ) near the image radius and assumed that this would be the value of the multiplicative bias on  $h$  a lens modeler would recover when fitting the system with a power-law profile. They found that the mean deviation of  $\lambda$  from unity can be as large as 20-50% with a scatter of 10-30% (rms). Even limiting their sample to the galaxies which recover a slope near isothermal resulted in a systematic deviation  $\sim 5\%$  with a scatter of 10%, implying that the power-law assumption introduces significant bias in the recovery of  $H_0$ . More recently, [Tagore et al. \(2018\)](#) performed a similar analysis using galaxies from the EAGLE simulation, with similar results. [Tagore et al. \(2018\)](#) continued their analysis by supplementing the lens systems with aperture velocity dispersion information. After using a joint model analysis and omitting lenses with poor  $\chi^2$ , they found that double image lenses were still biased at the 7% level. Quad lenses were less biased, with the cross quads specifically being the least biased at the 1.5% level (Table 7 and Figure 11 of [Tagore et al. \(2018\)](#)). It may yet turn out that the improvement and inclusion of kinematic information, combined with clever selection criteria, can help to mitigate the effects of the MSD.

Despite this finding, caution is advisable. Both [Xu et al. \(2016\)](#) and [Tagore et al. \(2018\)](#) extract lens profiles from state-of-the-art simulations, which may not have the resolution to describe the inner radii in sufficient detail. In particular, both studies selected galaxies with  $R_E \geq 2\epsilon$ , where  $\epsilon$  is the gravitational softening length of the simulation, and calculated slope and  $\lambda$  by using measurements at  $0.5R_E$ , i.e. as small as  $\epsilon$ . These findings are dependent on the simulations being well-resolved at just one softening length. This concern is exacerbated by the recent work of [van den Bosch & Ogiya \(2018\)](#). By analyzing a simplified case of a dark matter subhalo orbiting a static potential, they found that tidal disruption of subhalos within simulations is predominantly a numerical phenomenon rather than a physical process, implying even cutting-edge simulations may not be fully converged.

The goal of this paper is to quantify the bias and spread in the recovery of  $H_0$ , both with and without the inclusion of stellar kinematic constraints. Rather than drawing lens profiles from simulations, we will create lenses from two-component analytical profiles, constructed to represent both baryons and dark matter. Because of this, the true profile shape is well-known beforehand. The image positions and time delays will then be fit using a simple power-law ellipse+shear model, a common model for real systems. We will then compare the resulting slope and  $H_0$  with the expected value of  $s_\lambda$  and  $\lambda$  predicted by [Xu et al. \(2016\)](#). Such

agreement, which the authors assumed, would mean that it is possible to calculate the bias given the profile shape, while disagreement would mean that the MSD manifests in a more complicated way which is less straightforward to calculate.

In practice, stellar kinematic information can be used to provide an absolute measure of mass, breaking the mass-sheet degeneracy ([Suyu et al. 2014](#)). The effect is akin to setting the slope of the mass distribution to be the particular value which results in the required amount of mass at the inner radii of stellar dynamics. This extra information is hypothesized to reduce the bias and the spread of  $H_0$ . We will explore this hypothesis by testing the effects of constraining the slope in the parameter recovery, thereby emulating the additional constraint of kinematics.

Throughout this paper we will use  $h = H_0/100 \text{ km s}^{-1} \text{ Mpc}^{-1}$ . Lenses are constructed with  $h = 0.7$ .

## 2 PRELIMINARY TESTS

We will be modeling quads using the `lensmodel` application ([Keeton 2001](#)). The application inputs observational constraints combined with a choice of parametric model, then fits the system using the  $\chi^2$  calculated by comparing the modeled images to the observed constraints. This application has been used to model strong lens systems in a variety of studies (see [Lefor et al. \(2013\)](#) and references therein). Though `lensmodel` is capable of using image fluxes and extended images, we will simply evaluate  $\chi^2$  using image positions and time delays as our observable quantities, assuming optimistic observational uncertainties of 0.003 arcseconds in spatial resolution and 0.1 days in time delay measurements. The first step we must take is to confirm that we are able to accurately recover lens parameters from our mock quad images. We conducted several initial experiments to confirm this.

We wish to adopt a commonly-used analytical model with simplifying assumptions about the mass distribution of the lens. Specifically we choose to fit the lens with a ellipse+shear power-law model, which has 7 parameters: mass normalization, ellipticity, ellipse position angle, shear, shear angle, core softening radius, and slope. Since there are 9 observations (6 relative image coordinates and 3 relative time delays) there are  $9 - 7 = 2$  degrees of freedom.

Specific to `lensmodel`, we experimented with the `alpha` and `alphapot` models, which are a power-law mass distribution and lensing potential, respectively. Our preliminary tests were on several basic lenses, some matching the power-law forms of the fitting models and some using other profile shapes (namely the two-component Einasto profiles of [Gomer & Williams \(2018\)](#)). Limited to a cursory search using only a few quads, in some cases the lens parameters were successfully recovered. For other quads we were less successful, leading us to several main findings:

- (i) For some quads, fitting for two parameters in a different order resulted in a better or worse fit. This custom-tailored parameter search is only possible for a small number of quads modeled on an individual basis.
- (ii) Despite the optimization routine of `lensmodel`, the recovered slope frequently gets stuck at a local minimum near the initial slope guess. We also occasionally found that

restarts of the optimization routine would drastically depart from the nearby minimum and return bad fits.

(iii) Lenses created from power-law mass distributions (as opposed to lensing potential) had parameter recoveries which were worsened by pixelation and the finite window of lens construction.

(iv) Lenses created from Einasto mass distributions frequently had poor parameter recovery when assumed to be a power law. This is likely due to a combination of the numerical effect above and the MSD power-law assumption biasing the recovery of parameters.

We will have too many quads to model each in a unique way, such as customizing the order in which parameters are fit. Interestingly, this problem is becoming relevant for real lens systems as well, as the number of known systems continues to grow. Since human supervision is not feasible at this scale, automation must be the way forward. For real lens systems, automated fitting procedures such as Autolens (Nightingale et al. 2018) are already being developed. Our modeling is significantly less sophisticated, but will still require an automated algorithm which tries several different runs in `lensmodel` to find good fits for each quad in a uniformly controlled way.

Our fitting procedure is devised specifically to avoid the pitfalls of (i)–(iv). Here we define our method explicitly. The procedure is nearly identical to the example in Keeton (2001), with one extra step. The first run fits the quads with only the mass normalization free to vary, while searching a grid over all values for the position angle and shear angle. All other parameters are held at fiducial values for this first run. The robustness of this process against changes to these fiducial values is detailed in Appendix A. Next, a run is executed which uses the best fit result from the previous run as an initialization. This second run allows mass normalization, position angle, and shear angle to vary while searching a grid over values of ellipticity and shear. The third run initializes using the best-fit result of the second run and allows all 7 parameters to vary. This third run implements the “optimize” routine of `lensmodel`, which uses the `amoeba` algorithm available in Press et al. (1992), restarting several times to ensure that the result robustly returns to the same minimum. The last step is an additional step we have added to make sure the slope recovery does not get stuck at a local minimum. This step restarts the process at the first run, with a different initial value for the slope. Once the process is completed over the desired range of slope initializations, only the single result with the lowest  $\chi^2$  is kept. This result is the best fit for this model for a single quad, as the procedure systematically searches over the relevant parameters with a variety of initializations and restarts. To circumvent the problem arising from using mass distributions, from now on we will only construct lenses created via analytical lensing potentials, fit using a power-law potential via `alphapot`. This requirement means we can no longer use the Einasto form of the lenses constructed by Gomer & Williams (2018).

### 3 LENS CONSTRUCTION

Now that the numerical effects of the process have been limited to the best of our ability, we are ready to create our set of lenses. The lenses are constructed through the combination

of two components: a baryon power-law component and a dark matter NFW component, which is analytically expressible as a lensing potential (Golse & Kneib 2002; Meneghetti et al. 2003).

$$\phi = \phi_{bar} + \phi_{NFW} \quad (2)$$

where

$$\phi_{bar}(\xi) = b(r_c^2 + \xi^2)^{\alpha/2} \quad (3)$$

and

$$\phi_{NFW}(\xi/r_s) = 2\kappa_s r_s^2 f(\xi/r_s) \quad (4)$$

with

$$f(w) = \begin{cases} \ln^2 \frac{w}{2} - \operatorname{arccch}^2 \frac{1}{w} & (w < 1) \\ \ln^2 \frac{w}{2} + \operatorname{arccos}^2 \frac{1}{w} & (w \geq 1) \end{cases}$$

Ellipticity is introduced through  $\xi = (x^2 + y^2/q^2)^{1/2}$ , where  $q$  is the axis ratio of the potential. For the NFW component,  $w = \xi/r_s$  such that ellipticity is introduced in a consistent way, where  $r_s$  is the scale radius of the NFW profile. In total, five parameters are required to make a lens:  $b$ ,  $r_c$ ,  $\alpha$ ,  $\kappa_s$ , and  $r_s$ . The core softening radius,  $r_c$  is set to 0.3 kpc. Note that the 2D slope of the power-law mass distribution will be equal to  $\alpha - 2$ .

The cornerstone of the interpretation of Xu et al. (2016) is that the value of  $\lambda$  calculated from the radial profile will be equivalent to the bias on  $h$ . To test this, we experiment with a few different sets of values for the four parameters which go into making our lenses (baryon normalization,  $b$ , and slope,  $(\alpha - 2)$ , as well as dark matter normalization,  $\kappa_s$ , and scale radius,  $r_s$ ) to create a few different values of  $\lambda$  and see how  $h$  is recovered in all cases. The choice of profile is somewhat difficult, since many options are physically reasonable. We settle on four different parameter choices of this class of profile, plotted in Figure 2 with their values summarized in Table 1. While all of these four models are comparable to real galaxies, we consider Model D to be the best analog due to its slope being slightly steeper than isothermal which is in good agreement with real halos (Barnabè et al. 2011). Meanwhile, Model A represents the most drastic departure from a power-law model, as evidenced by its visible curvature.

The process to calculate  $\lambda$  and  $s_\lambda$  is quite simple: choose a region near the Einstein radius ( $R_E$ ) over which the slope,  $s$  is calculated. The magnitude of the mass sheet transformation (MST) necessary to transform the profile into a power law within that chosen region is  $\lambda$ , while the corresponding new slope after the MST is  $s_\lambda$  (Equations 4 and 10 of Xu et al. (2016)).

One subtlety here is that the bounds over which the calculation is done are somewhat arbitrary—Xu et al. (2016) and Tagore et al. (2018) use  $0.5R_E$  and  $1.5R_E$  and these are the bounds used for the values calculated in Table 1, but other choices for the bounds are no less valid. Because the slope changes with radius, other choices for the bounds return different values of  $s$ ,  $\lambda$  and  $s_\lambda$ . This will be further explored shortly.

For a given model, 100 lenses are created, each producing 1 quad. Each lens is given an axis ratio between 0.85 and 0.99 in the potential, which roughly corresponds to between 0.5 and 0.99 in mass. This range is motivated because values more extreme than  $\approx 0.85$  in potential results in mass

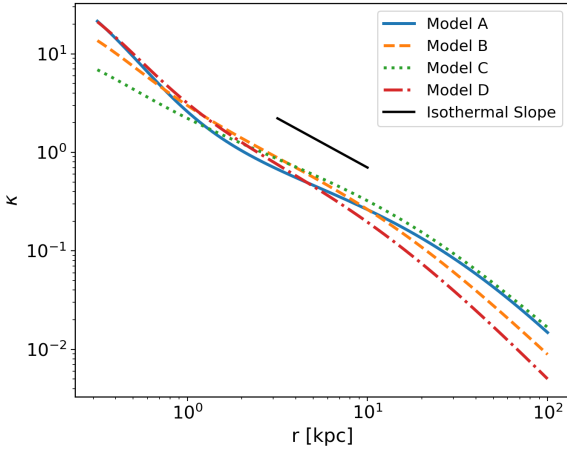


**Figure 2.** The radial profiles are plotted for the four models. The Einstein radius for each model is set to  $\approx 5$  kpc. Note that while models do vary in exact shape, they have approximately isothermal slopes near the image radius. We construct these halos analytically as opposed to extracted from simulations, because the gravitational softening length  $\epsilon$  of state-of-the-art simulations is about 0.7 kpc (EAGLE, Illustris). Based on Figure 9 of Power et al. (2003), halos may not be fully resolved until radii  $2\text{--}3\epsilon$  outward, meaning simulations cannot reliably detail the nuances of the profile shape interior to about 2 kpc.

distribution contours which become “peanut-shaped” rather than elliptical. The 100 quads are then fit by the automated process in Section 2, returning values for the 7 parameters,  $\chi^2$ , and  $h$ .

We intentionally choose to fit the lens systems with a model (power law) that does not have the same shape as the density profile (NFW + power law). In real systems, the true mass profile of an individual lens is not directly observable, but some model is assumed based on other studies of a population of galaxies. No individual galaxy will perfectly match the model profile, so this is always the case to some degree. Most studies assume that if the image positions are reproduced, then the lens model sufficiently matches the true mass distribution, but Schneider & Sluse (2013) found that this effect can result in significant bias on  $h$ . Since we can never have perfect knowledge of what the correct profile shape is, the effect of our ignorance must be included when seeking to evaluate our ability to fit lensing parameters.

## 4 RESULTS

We are primarily interested in the statistical results of an array of quad systems. Nonetheless, we have more deeply explored a particular quad from Model D to make certain that the image positions and time delays are properly recovered. We share these fittings in Appendix B. Confident that our procedure works, we are ready to discuss the results of the population.

### 4.1 Parameter recovery: density slope free to vary

The most straightforward way to represent the results is to plot a histogram of the best-fit values of slope and  $h$ , shown in Figure 3 as the blue distribution for each of the four models. Nearly all fits returned  $\chi^2/dof < 1$ . The few cases with bad fits are omitted from these plots, meaning all of the recovered parameters in the figure are within the uncertainties of observations. As an additional test of modeling success, we checked to see if the recovered ellipticities are strongly correlated with the true ellipticities, and find a Pearson coefficient  $R \approx 1.0$  after omitting the few cases with  $\chi^2/dof > 1$ . Our lenses have zero input shear, and the recovered shear values are nearly zero. This tells us that not only do the image positions match, but the mass model parameters correspond quite well to their true values. These measures of fitting success are included in Table 2.

While useful, the blue histograms in Figure 3 do not fully capture the process of determining a single value of  $h$  from many quads. As the number of systems increases, the shape of the blue distribution will stay roughly the same and will not narrow (see Appendix A), as it only returns a single value for each quad and does not combine them together in any way. Meanwhile, determinations of  $h$  such as those presented by Wong et al. (2019) and Tagore et al. (2018) represent posterior distributions of  $h$  from a single system, as well as aggregated together for a composite distribution from a number of systems.

To evaluate this, we use the `varyh` function in `lensmodel` to calculate the  $\chi^2$  for a range of  $h$  values near the best-fit value, marginalized over the other fitting parameters. We then calculate a likelihood for each quad and combine the likelihoods together to evaluate the  $h$  corresponding to the maximum likelihood estimation (MLE). To quantify the variance of this estimator, we bootstrap the distribution using subsets of 50 quads and evaluate 2000 realizations. The green curve in Figure 3 represents a Gaussian fit to the resulting distribution. This curve more accurately depicts the resulting bias and scatter one would get from combining 100 systems together into a single determination of  $h$ . Table 2 lists these quantities for each model.

Across the four models, the distribution of the best-fit  $h$  values (blue histogram, Fig. 3) has a scatter  $\gtrsim 10\%$ . As anticipated, combining the fits using the MLE determination of  $h$  (green Gaussian) has a much narrower scatter,  $\sim 3\text{--}4\%$ .

Our main result of this section is that the median recovered values for slope and  $h$  do not consistently match the predicted values corresponding to the MST anticipated by Xu et al. (2016) (orange dashed line, Fig. 3). For  $h$  in particular, the predicted bias of  $\lambda$  should be compared with the MLE result (green Gaussian), and is inconsistent for all but Model D. For the other three models, the prediction misses the mark by 10%–18%. In some cases,  $\lambda$  underpredicts the magnitude of the bias while in others it overpredicts the magnitude. In both Models B and C, the direction of the bias is incorrectly predicted, failing to even outperform the naive assumption that  $h$  will be unbiased (solid black line). Even in Model D, where  $\lambda$  is consistent with the MLE result, it misses the mean by about 2%, which is a significant problem when one considers the 1% goal.

The capacity of  $s_\lambda$  to match the recovered value of slope is no more successful. We did not calculate the MLE with

| Profile construction parameters |          |                            |                   |            | Resulting lens physical attributes |                         |   |                           |                       |     | MST values |           |             |
|---------------------------------|----------|----------------------------|-------------------|------------|------------------------------------|-------------------------|---|---------------------------|-----------------------|-----|------------|-----------|-------------|
| Model                           | $\alpha$ | $b[\text{kpc}^{2-\alpha}]$ | $r_s[\text{kpc}]$ | $\kappa_s$ | $R_E[\text{kpc}]$                  | $R_{trans}[\text{kpc}]$ | $\frac{\Sigma_{DM}}{\Sigma_{total}} _{R_E}$ | $M_{200}[\text{M}_\odot]$ | $r_{200}[\text{kpc}]$ | $c$ | $s$        | $\lambda$ | $s_\lambda$ |
| A                               | 0.30     | 30.0                       | 30.0              | 0.12       | 5.1                                | 1.7                     | 0.81  | $2.5 \times 10^{12}$      | 103                   | 3.4 | -0.830     | 1.06      | -0.94       |
| B                               | 0.60     | 10.07                      | 13.33             | 0.206      | 5.7                                | 2.1                     | 0.67  | $1.6 \times 10^{12}$      | 77                    | 5.8 | -1.03      | 0.925     | -0.895      |
| C                               | 0.816    | 3.76                       | 22.25             | 0.157      | 4.9                                | 1.6                     | 0.68  | $2.7 \times 10^{12}$      | 95                    | 4.3 | -0.815     | 0.904     | -0.702      |
| D                               | 0.40     | 22.53                      | 10.0              | 0.225      | 5.5                                | 2.0                     | 0.70  | $1.0 \times 10^{12}$      | 66                    | 6.6 | -1.14      | 0.960     | -1.05       |

**Table 1.** The characteristics of the four lens models shown in Figure 2. First, the parameters used to construct the different lens profiles are presented (outlined in Section 3). The next set of numerical values correspond to physical features of each lens profile: the Einstein radius, the radius at which the surface density profile transitions from being dominated by baryons to being dominated by dark matter, the local dark matter fraction at the Einstein radius in 2D projection, the virial mass and virial radius, and the concentration. Calculations of relevant physical quantities assume a lens redshift of 0.6. Finally, the values associated with the MST formalism of Xu et al. (2016) are calculated:  $s$ , the slope calculated by using  $0.5R_E$  and  $1.5R_E$  as the endpoints;  $\lambda$ , the value required for the mass-sheet transformation to make the profile a power law over the corresponding radii; and  $s_\lambda$ , the resulting slope of the transformed profile, which should be the value recovered by the fitting software through the power-law assumption. The values of  $s$ ,  $\lambda$ , and  $s_\lambda$  are simply for comparison purposes and are not used in the fitting process.

| Parameter recovery: density slope free to vary |           |                   |           |                      |
|--|-----------|-------------------|-----------|----------------------|
| Model  | $\lambda$ | MLE $h$           | $R_{ell}$ | $f_{\chi^2/dof} < 1$ |
| A  | 1.06      | $1.162 \pm 0.026$ | 1.00      | 0.99                 |
| B  | 0.925     | $1.064 \pm 0.046$ | 0.99      | 0.99                 |
| C  | 0.904     | $1.084 \pm 0.036$ | 1.00      | 1.00                 |
| D  | 0.960     | $0.986 \pm 0.031$ | 1.00      | 0.97                 |

**Table 2.** The results are presented for the recovery of  $h$  when the slope is free to vary in the fitting process. The distribution of  $h$  values relative to the correct value, recovered from the MLE, are presented with  $1\sigma$  uncertainties. A value of 1.0 corresponds to an unbiased recovery of  $h$  while for example a value of 0.986, as in Model D, corresponds to a 1.4% bias downward. This should be compared to  $\lambda$ , which Xu et al. (2016); Tagore et al. (2018) assumed would be the bias in the recovery of  $h$  based on the argument that the profile will be transformed into a linear slope over the region between  $0.5R_E$  and  $1.5R_E$  via the mass-sheet degeneracy. One of our main findings is that the distribution of  $h$  does not seem to be related to  $\lambda$ , indicating this estimate of bias is not accurate. Also presented are two measures of goodness of fit:  $R_{ell}$  represents the Pearson correlation between the recovered value of ellipticity and the true value, with a strong correlation meaning that the parameter is recovered well in most cases, while  $f_{\chi^2/dof} < 1$  represents the fraction of systems which were successfully fit within the uncertainties of real observations. Cases with poor fits are heavily downweighted through the MLE process and are explicitly omitted when determining  $R_{ell}$ .

respect to slope as our main quantity of interest is  $h$ . Additionally, to do so would be to assume all quads come from the same profile, which is not true in general. We can only compare to the blue distribution of best fit values. In all but Model A,  $s_\lambda$  (orange dashed line) makes a worse prediction than the untransformed slope (solid black line).

One manifestation of the MSD is a relationship between the steepness of a lens profile and the estimate for  $h$ . This is subtle, but present in Figure 3, where the general shapes of the blue distributions for slope and  $h$  are more or less mirrored, with steeper profiles resulting in a higher  $h$ . We will explore this effect more thoroughly in the next section.

## 4.2 Parameter recovery: fixed slope

The fully automated method allows the slope to vary when recovering the parameters, but it is also useful to note the results when the slope is fixed. Fixing the slope at a particular value is an act of utilizing additional information which breaks the mass sheet degeneracy. In the context of real lenses, this information can come from the inclusion of stellar kinematics, which probe the mass at radii near the images. When combined with lensing mass estimates, constraints are effectively placed on the profile slope. A truly complete analysis of this effect would be to include a model for stellar kinematics and simultaneously fit velocity dispersion data with the image positions to recover lens parameters. This is beyond the scope of this paper, but we are still interested in the general effect that arises from knowing information about the slope, and fixing the slope at a particular value approximates the effect.

The question then becomes what value to fix the slope to. Is the ‘‘correct’’ value the one which the true mass distribution follows ( $s$ ), the one which corresponds to the slope after the MST molds the profile into a power law ( $s_\lambda$ ), or some other slope? An additional complication is that the value for each is dependent on the bounds over which the slope is calculated. Which of these values, if any, will result in zero bias on  $h$  recovery? To explore this question, allow us to focus on Model D; we will return to the other models later in this section.

We ran a similar test as the ones before, with 100 realizations of the Model D profile, but this time constraining the slope to be -1.1. This value is chosen because it is close to both  $s$  (-1.14) and  $s_\lambda$  (-1.05) one would calculate using  $0.5R_E$  and  $1.5R_E$  as the bounds. Fewer quads are fit with acceptable  $\chi^2/dof$  (69/100) but the correlation between model ellipticity and true ellipticity is still very strong. Again combining the fits together into an MLE determination of  $h$ , the recovered value of  $h$  is now considerably biased (-11.5%, Table 3). Since slope and  $h$  are strongly linked, we interpret this result to mean that the value of slope used here is not the value which would result in zero bias on  $h$ . There must exist some value of slope which results in an unbiased  $h$ , but lensing degeneracies have manifested through the modeling process in some way causing this value to be different from what we anticipated. This prompts us to consider the value of the slope more carefully.

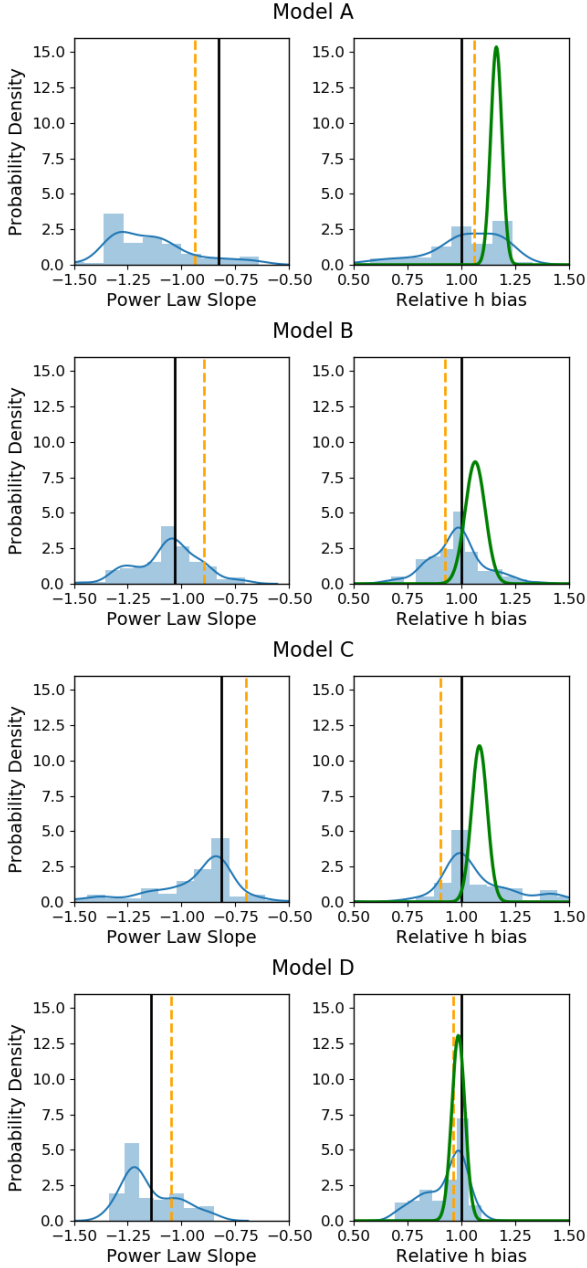


**Figure 3.** Recovered distributions of power-law slope and  $h$  (scaled such that 1.0 is unbiased) are presented after 100 quads are fit for each model. The blue curve/histogram represents a Gaussian kernel density estimation of the distribution of each best-fit  $h$  value. Cases with poor  $\chi^2/dof < 1$  are omitted. The green curve represents the result when combining the likelihoods of each quad together into one estimate of  $h$ . A Gaussian estimation of error is obtained through the bootstrap process detailed in Section 4.1. The black solid lines represent the untransformed value of the slope and unbiased value of  $h$ , while the orange dashed lines represent the values of  $s_\lambda$  (left panels) and  $\lambda$  (right panels) calculated by assuming a mass-sheet transformation morphs the profile into a power law over the relevant region. The scatter on  $h$  evaluated through the MLE is  $\approx 3\%$ , while the median bias ranges from 2% to 16% depending on the model (see Table 2). The median bias does not appear to be well-described by  $\lambda$ , contrary to the expectation of Xu et al. (2016); Tagore et al. (2018).

Since the slope of the profile is changing with radius, it is not immediately clear what slope `lensmodel` should recover. The value of the slope near the Einstein radius is dependent on the choice of the two points used to calculate it. Figure 4 shows the effect of changing these bounds on the calculated values of slope,  $\lambda$ , and  $s_\lambda$ . Generally, choices which are symmetric about the Einstein radius recover values of  $s$  between -1.1 and -1.3 for Model D. It is not obvious which value is the correct one to fix the slope to when recovering parameters in the “fixed slope” case. It is therefore prudent to run the “fixed slope” test for all values in this range, and see which results in the least-biased value of  $h$ . The resulting recoveries of  $h$  are depicted in Figure 5. The MSD is illustrated by a clear trend, where a steeper slope results in a higher value of  $h$ . The slope value which results in no bias happens to be about -1.25, which is quite different from the value one would calculate using  $0.5R_E$  and  $1.5R_E$ , although similar to the median value in Figure 3 (bottom left).

We run this same test for all four models, holding the slope fixed at different values. The results are listed in Table 3. The values of slope which result in the least bias are in bold, while the values with slope closest to  $s$  are italicized. In all but Model B, these two values are different. The choice of color scheme for Figure 4 is now clear, where we have set the white region to the value of the slope which results in no bias. This makes it clear which choices for the bounds on the definition of slope result in the zero-bias value. With the slight exception of Model B, the choice of bounds using  $0.5R_E$  and  $1.5R_E$  (green cross) is quite removed from the white portions of the figure, indicating this choice of values results in a biased estimation of  $h$ .

When the slope is held fixed at a particular value, the scatter of the distribution of  $h$  is reduced to  $\sim 2\%$ , depending on the model and value of slope chosen. This is still too much scatter for a 1% determination, but it may be that the spread would be further reduced in the case of finite source size. We are more concerned with the bias, which has a strong relationship with the recovered slope: a shallower slope biases  $h$  low, while a steeper slope biases  $h$  high. In all cases, the value for the slope which results in minimal bias on  $h$  is steeper than both  $s$  and  $s_\lambda$ . When the slope is held at values closer to  $s$  or  $s_\lambda$ , the recovered value of  $h$  is less than it should be. This result in relation to the role of kinematics is discussed in the next section.

## 5 DISCUSSION

The motivation of this exploration has been to determine the reliability of the analytical calculation of  $\lambda$  using the density profile shape near the Einstein radius as an estimator of  $h$ . As illustrated in Figure 3, the distribution of recovered values of slope and  $h$  do not correspond to the values predicted using the arguments of Xu et al. (2016). Generally, the distribution of  $h$  is no better matched by the predicted bias,  $\lambda$ , than it is by blindly assuming no bias is present on  $h$ . Similarly, the mass-sheet-transformed  $s_\lambda$  is no better than the untransformed slope,  $s$ , as an indicator of the recovered slope. We see no clear way to predict the bias of  $h$  directly from a profile aside from creating and fitting many lens systems.

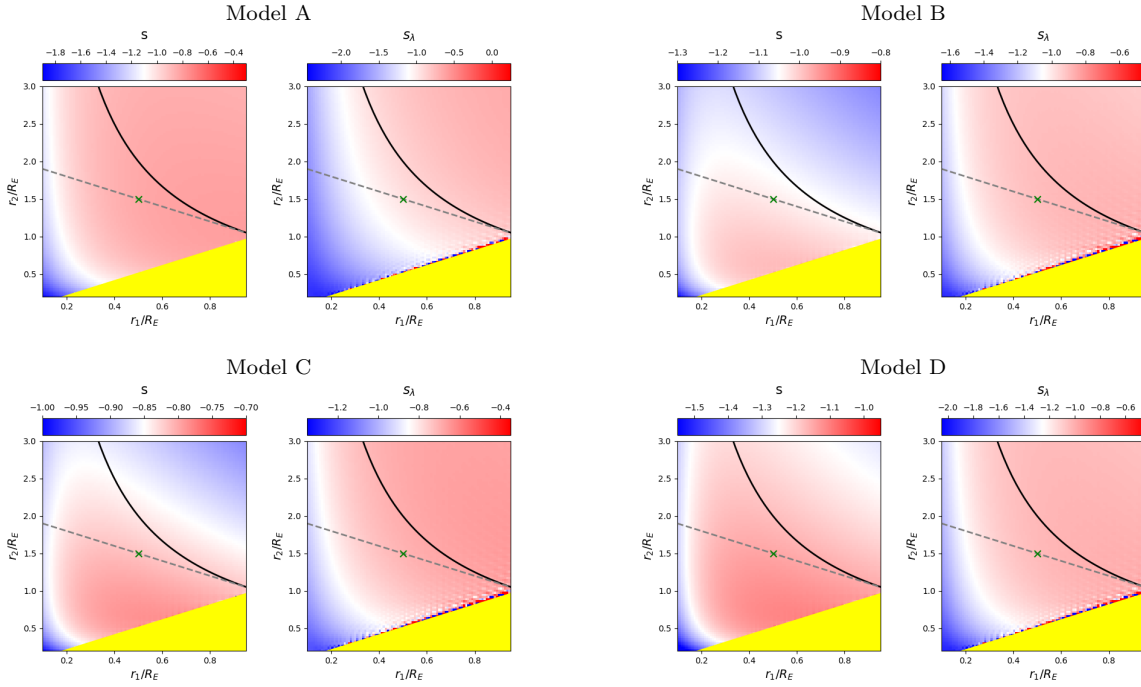


**Figure 4.** The choice of region over which the slope is calculated impacts the measured slope,  $s$ , as well as the mass-sheet transformed slope required to make the profile linear over the region,  $s_\lambda$ . For each of the four models, vertical and horizontal axes represent the upper- and lower-bound choice for radius within which the slope is calculated,  $r_2$  and  $r_1$  respectively. Since the upper bound must be greater than the lower, the yellow region is non-physical. Shaded color represents the resulting value of  $s$  and  $s_\lambda$ . Note that the range of values is different for each and indicated by the color bar in each panel. The colors are set such that the white regions correspond to  $s$  and  $s_\lambda$  which result in nearly zero bias (listed for each model in Table 3). The black solid line represents the choices of bounds which are logarithmically spaced around the Einstein radius, while the gray dashed line indicates bounds which are linearly spaced. Xu et al. (2016); Tagore et al. (2018) chose the bounds indicated by the green “X.” The main feature of note is that most reasonable choices of bounds spanning the Einstein radius result in a biased value of  $h$  for all four models.

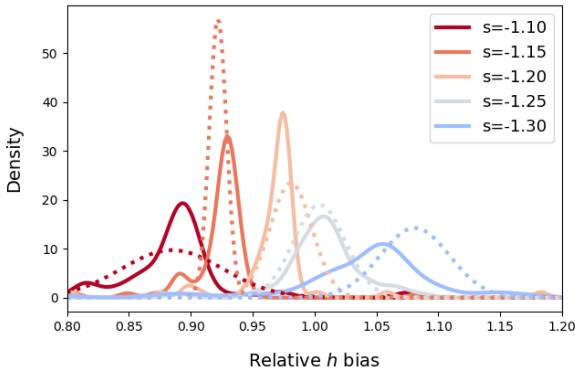


**Figure 5.** The recovery of  $h$  for Model D when the slope is fixed at different values, with colors corresponding to the range of values in Fig. 4. For each value at which the slope is held, the distribution of best fit values of  $h$  is represented as a solid curve. The dotted Gaussian curves represent the range of values recovered when the fits are combined together and  $h$  is calculated through an MLE. Fixing the slope to be steeper results in a higher  $h$ . The value which corresponds to no bias in  $h$  (slope  $\approx -1.25$ ) is not the same as either the measured MSD slope of the mass distribution or the calculated slope after an MST is applied (both  $\approx -1.1$  for this model).

We find this result perplexing, as we found the logic of Xu et al. (2016) convincing. We expected that the effect of the mass sheet degeneracy would be to transform the slope into the one which fits the assumed model over the relevant radii. Instead, it appears the degeneracy manifests in a more complicated way. The MSD, or perhaps even some combination of degeneracies, has created minima in the parameter space which do not correspond to the MSD expectation alone.

Beyond this conclusion, our experimentation with constraining the slope has uncovered some interesting results. First, we confirm the relationship between  $h$  and slope, where a steeper mass distribution results in a higher value of  $h$ , a known consequence of the MSD. More interestingly, we find that the slope corresponding to the mass profile near the Einstein radius results in a biased  $h$ . In other words, even when we give the fitting the “right answer” for the density slope it does not result in an unbiased  $h$ . This merits a discussion of what it actually means when we constrain the slope, what the “right answer” really means, and how this applies to the physical analog: the inclusion of stellar kinematic information.

### 5.1 Kinematic constraints

When stellar kinematics are included, the profile is probed at a range of radii depending on the spatial resolution of the kinematic information. The exact location of this region



| Model A      |                                     |             |                      |
|--------------|-------------------------------------|-------------|----------------------|
| Slope        | MLE $h$                             | $R_{ell}$   | $f_{\chi^2/dof} < 1$ |
| -0.85        | $0.769 \pm 0.023$                   | 0.97        | 0.67                 |
| -0.90        | $0.817 \pm 0.027$                   | 0.98        | 0.70                 |
| -0.95        | $0.859 \pm 0.013$                   | 0.98        | 0.71                 |
| -1.00        | $0.907 \pm 0.019$                   | 0.98        | 0.72                 |
| -1.05        | $0.965 \pm 0.016$                   | 0.97        | 0.58                 |
| <b>-1.10</b> | <b><math>1.016 \pm 0.023</math></b> | <b>0.99</b> | <b>0.64</b>          |
| -1.15        | $1.078 \pm 0.028$                   | 0.99        | 0.60                 |
| Model B      |                                     |             |                      |
| Slope        | MLE $h$                             | $R_{ell}$   | $f_{\chi^2/dof} < 1$ |
| -1.00        | $0.944 \pm 0.011$                   | 0.99        | 0.60                 |
| <b>-1.05</b> | <b><math>0.975 \pm 0.014</math></b> | <b>0.97</b> | <b>0.64</b>          |
| -1.10        | $1.037 \pm 0.055$                   | 0.99        | 0.55                 |
| -1.15        | $1.097 \pm 0.018$                   | 0.99        | 0.69                 |
| Model C      |                                     |             |                      |
| Slope        | MLE $h$                             | $R_{ell}$   | $f_{\chi^2/dof} < 1$ |
| -0.80        | $0.960 \pm 0.007$                   | 0.98        | 0.70                 |
| <b>-0.85</b> | <b><math>1.023 \pm 0.008</math></b> | <b>0.98</b> | <b>0.64</b>          |
| -0.90        | $1.067 \pm 0.019$                   | 0.97        | 0.65                 |
| -0.95        | $1.130 \pm 0.018$                   | 0.99        | 0.69                 |
| Model D      |                                     |             |                      |
| Slope        | MLE $h$                             | $R_{ell}$   | $f_{\chi^2/dof} < 1$ |
| -1.10        | $0.885 \pm 0.041$                   | 0.99        | 0.69                 |
| <i>-1.15</i> | <i><math>0.922 \pm 0.007</math></i> | <i>0.99</i> | <i>0.68</i>          |
| -1.20        | $0.981 \pm 0.017$                   | 0.97        | 0.62                 |
| <b>-1.25</b> | <b><math>1.004 \pm 0.021</math></b> | <b>0.97</b> | <b>0.55</b>          |
| -1.30        | $1.081 \pm 0.028$                   | 0.99        | 0.67                 |

**Table 3.** Resulting recovery of  $h$  when power-law slope is fixed at a particular value, scaled such that a value of 1.0 corresponds to an unbiased recovery of  $h$ . The value of the slope which results in the least bias is highlighted in bold, while the value of the slope which is closest to that of the true mass distribution in the region between  $0.5R_E$  and  $1.5R_E$ ,  $s$ , is italicized. In all but Model B, these slope values do not coincide. The predicted value of slope after an MST,  $s_{\lambda}$  (see Table 1), is even farther away from the zero-bias values for all but Model A.

is somewhat complicated to evaluate, as in reality the data in each pixel is weighed according to its S/N (Czoske et al. 2008), but the approximate effect is to measure the average slope within the region. This information is used to break the MSD by constraining the model to have this particular slope. Since we are using a power-law model fit for the lens, this slope constraint is set as the slope for all radii, while in reality the slope changes with radius. This means that the value which the stellar kinematic data recover will depend on the region being probed. We stress that though we are using specific profiles for the true and model profiles, this conclusion applies in general because the true and model profiles will never be identical. Specific to our profiles, we return to Figure 4 (left panels), which shows the average slope of each profile given the two radii,  $r_1$  and  $r_2$ , used to calculate it. To recover an unbiased value of  $h$ , the slope has to be measured between the particular radii which result in the white portions of the figure. If stellar kinematics surveys correspond to these regions, the recovered value of  $h$  will be reliable, but if they correspond to a red or blue portion, bias will result.

It is possible that real halos are more similar to Model B than Model D. The former has a slightly shallower profile,

and is nearly isothermal at the image radii. For the Model B profile, when  $r_2$  is greater than  $2R_E$ , the determined slope results in a value of  $h$  which is biased high (blue portion in the left panel of Fig. 4). We speculate that such a bias could result if stellar kinematic constraints used in the H0LiCOW analysis (Wong et al. 2019) are obtained from these regions of the lens ( $r > 10$  kpc), and would lead to an overestimation of  $H_0$  compared to the CMB (Planck Collaboration et al. 2018) and TRGB values (Freedman et al. 2019).

It is interesting to note that for each model, there appears to be a region near  $r_1 = 0.15R_E$  which results in an unbiased slope. The white region is a nearly vertical strip here, indicating that the value of  $r_2$  is less important. The fact that this is consistent across all four models may imply that there may be something special about this determination of slope. In Figure 2 this corresponds to using  $r_1 = 0.75$  kpc. It seems feasible by eye that the slope between this radius and, for example, the Einstein radius (5 kpc), reasonably accounts for the baryon component of the profile yet also approximates the slope of the dark matter at farther radii. If  $r_1$  were smaller the slope would be too steep at farther radii, but if  $r_1$  were larger the slope would be too shallow at inner radii. It appears to be a mathematical coincidence, but a consistent one. It may be that if the spatial resolution of stellar dynamics studies can reach this region, the constraint will result in an unbiased value of  $h$ .

At present, state-of-the-art measurements are insufficient to spectroscopically resolve this region. H0LiCOW (Wong et al. 2017) used 1D spectra from Keck/LRIS to constrain their HE 0435–1223 determination of  $H_0$  with a seeing of  $0.8''$  (5.3 kpc at  $z = 0.6$  or  $1.1R_E$  in Fig. 4). Czoske et al. (2012) obtained two-dimensional kinematic data of SLACS lenses using the VLT/VIMOS IFU with a spatial resolution of  $0.67''/\text{pixel}$  (4.4 kpc,  $0.9R_E$ ). To reach  $0.15R_E$ , a resolution of  $0.1''$  is necessary. It could be that this region can be probed without spatially resolving it, since the innermost regions of the galaxy will be brighter and contribute greatly to the S/N of the innermost pixel. Exactly how this enters into the kinematic constraint will depend on how the pixels are weighted, which is outside the scope of this paper.

Unless this region can be reliably probed, the value of  $h$  resulting from stellar kinematic constraints will not be unbiased. In fact, if the degeneracy is broken using a different slope, it may introduce more bias than simply not including stellar kinematics at all. For example, Model D returned  $h = 0.986$  when the slope was free to vary but  $h = 0.922$  when the slope was held at -1.15, the value of the true slope near the Einstein radius. Future surveys should consider an analysis without including stellar kinematics, which will increase the scatter in  $h$  but may be less biased.

## 5.2 Subsample selection

As a final investigation, we are curious if there exists a subset of quad systems which have distributions of  $h$  with either less bias or less scatter. To be useful, this selection would need to be based on an observable quantity independent of the modeling process. Tagore et al. (2018) explored the effect of quad configuration (e.g. cusp, fold, and cross) on the recovery of  $h$  and found that cross lenses had the least bias. We adopt the notation of Woldesenbet & Williams (2012), who investigated the angular positions of quad images, wherein

the polar image angle between the second- and third-arriving images,  $\theta_{23}$ , serves to represent quad configuration (fold and cusp quads have  $\theta_{23} \approx 0$ , while cross quads have  $\theta_{23} \approx 90^\circ$ ). In order to see trends in the MLE determination of  $h$  with respect to  $\theta_{23}$ , it would be necessary to bin the data, which would in turn reduce the sample size so low as to make the MLE error estimation unreliable. Instead, we simply create scatter plots of the best fit  $h$  for each quad versus  $\theta_{23}$  (left panels of Figure 6). There does not appear to be a significant reduction in scatter or bias for cross quads as opposed to others.

While we did not find dependence on the type of quad, we also explored dependence on the radial positions of quad images. The right panels of Figure 6 show that quads which have images over a larger range of radii  $\Delta r/R_E > 0.2$  have less scatter in their recoveries of  $h$  than those with a more confined range of image radii. To quantify this, we calculated the distributions of  $h$  if one selects only quads with  $\Delta r/R_E > 0.2$ , to be compared with the blue histograms in the right panels of Figure 3. This selection of quads returns  $h = 1.177^{+0.028}_{-0.171}$  for Model A,  $h = 0.995^{+0.142}_{-0.073}$  for Model B,  $h = 0.990^{+0.183}_{-0.035}$  for Model C, and  $h = 0.991^{+0.016}_{-0.018}$  for Model D.

For all models, the amount of scatter has decreased, most drastically for Model D and only marginally for Model B. It follows that a quad which probes a range of radii has less freedom in the fitting process and correspondingly less scatter in  $h$ . For Model A, the median has changed substantially, while for the other models the median has changed at the 1-2% level. It is unclear why the quads which probe a range of radii in Model A would be more biased than the other models, but is likely related to the fact that Model A has the profile with the most drastic curvature i.e. departure from the power-law model (visible in Fig. 2). The utility of making this selection in real surveys is questionable unless this biasing effect can be understood.

### 5.3 Limitations to this study

There are clear limitations to this study. Only four variants on a similar profile have been tested, hardly enough to draw sweeping conclusions about all mass distributions. It is possible that  $\lambda$  could better quantify the bias on  $h$  in other cases. Xu et al. (2016) also note that the MST can be calculated to transform the profile into a power law with respect to deflection angle rather than convergence, with a corresponding bias of  $\bar{\lambda}$ . We have focused on the convergence power law, and so this deflection angle MST argument remains untested. Comparing this work to Tagore et al. (2018), more quads were successfully fit with small  $\chi^2$ , but our work uses simple elliptical profiles with no lens environments or such complications. Discrepancies from an elliptical shape are prevalent in real lenses (Woldesenbet & Williams 2015; Gomer & Williams 2018), although the effect of such complexities on the recovery of  $h$  is unknown. This topic will be further explored in a coming paper. Tagore et al. (2018) also examined mock lenses over different redshifts, while all lenses in this study are at the same redshift. Finally, our interpretation regarding the slope constraint is that stellar kinematic constraints are equivalent to holding the slope at the weighted average value over the radii of the kinematic

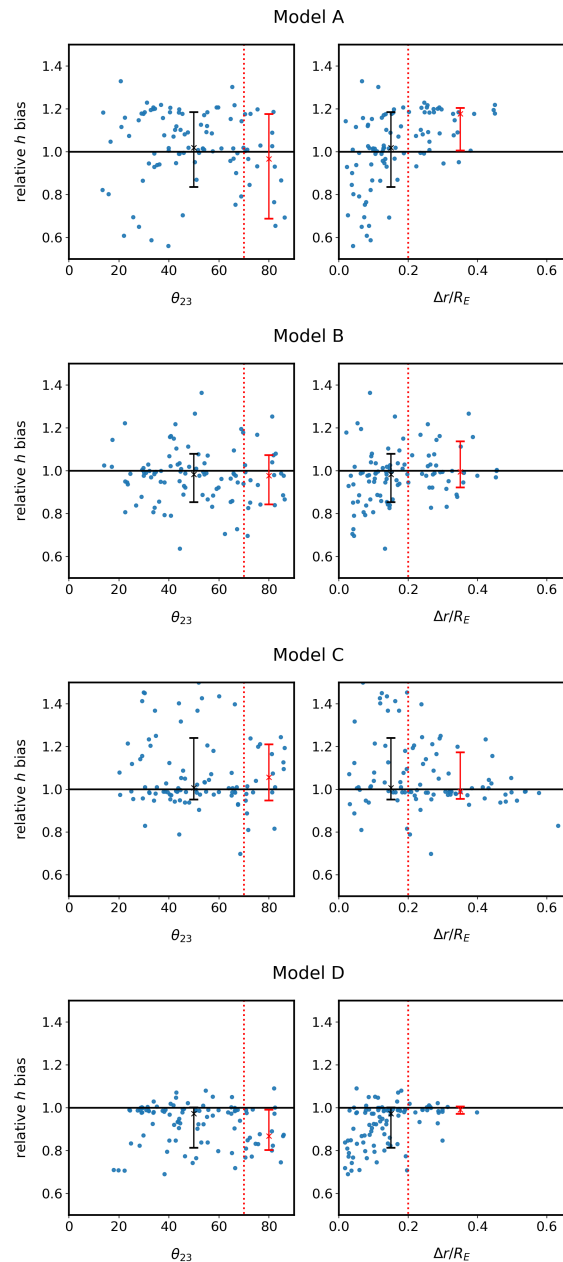


**Figure 6.** Scatter plots of the recovered best-fit values of  $h$  for each quad against quad orientation (left) and image radial range (right). For each model, the left panel plots  $h$  against  $\theta_{23}$ , the polar angle between the second- and third-arriving images, which denotes cusp/core quads (small  $\theta_{23}$ ) from cross quads ( $\theta_{23} \approx 90^\circ$ ). The black cross with error bars denotes the median and spread of the full set of quads, while the red cross with error bars indicates that of the cross quads: only quads with  $\theta_{23} > 70^\circ$  (right of the red dotted line). There does not appear to be a significant change in the distribution of  $h$  between different quad types. The right panel plots  $h$  against the radial range over which the images span,  $\Delta r/R_E$ . Again the black cross with errors indicates the same bias and spread of the whole population, while this time the red cross with error bars specifically refers to the quads with  $\Delta r/R_E > 0.2$  (again right of the red dotted line). Quads which span a greater range of radii tend to have less scatter in their recovered values of  $h$ . Quads with poor recoveries ( $\chi^2/dof > 1$ ) are omitted from these plots.

measurement. This interpretation needs to be confirmed in a study which incorporates kinematics into the fitting. This is especially relevant given that one of our main findings is that lensing degeneracies are less predictable than our intuition implies.

## 6 CONCLUSION

Gravitational lensing is a competitive method for measurement of  $h$  to 1% precision independent of the distance ladder or the CMB. To reach this goal, degeneracies inherent to lens modeling must be precisely quantified and accounted for. To explore the effects of lensing degeneracies on  $h$  recovery, we constructed quad lens systems from a series of two-component profiles, then fit these quads with a model different from the true profile: a power-law model. We then determined recovered distribution of  $h$  values and compared them to the analytical predictions of Xu et al. (2016).

Our first finding is that the bias (location of the median) of the distribution of  $h$  does not correspond to the value of  $\lambda$  predicted by the mass-sheet transformation arguments in Xu et al. (2016) and Tagore et al. (2018). Lensing degeneracies have conspired in an unexpected way to return unanticipated values of  $h$ . Any attempt to statistically quantify the bias on  $h$  using simulated galaxies cannot be analytically calculated from lens profiles, but instead must be painstakingly recovered through the creation of mock quads fit with software.

We further explore the effect of the inclusion of stellar kinematics by constraining the slope in the fitting process, which emulates the process by breaking the MSD through the inclusion of external information. We find that when the slope is held to the true value of the slope near the Einstein radius,  $h$  can be considerably biased (0-8% for Models B,C, and D). Strangely, the addition of the correct information has caused the fitting to return an incorrect value. The value of slope which results in no bias on  $h$  does not correspond to the true slope, perhaps indicating that “slope” acts as fitting parameter rather than describing the physical slope of the density profile. The inclusion of kinematics breaks the degeneracy, but can do so incorrectly, so as to introduce a significant bias.

A remarkable consistency across all four of our models is that when the inner radius used in the determination of slope,  $r_1 \approx 0.15R_E$ , the calculated slope results in zero bias in  $h$ , insensitive to the outer radius,  $r_2$ . If the spatial resolution of kinematic surveys can be increased to probe this region, the constraints placed by such measurements would not introduce a bias on  $h$ . At present such inner radii are out of reach. It may be possible to explore this region through simulations, although the resolution of modern simulations is insufficient, with  $0.15R_E \approx 0.9\epsilon$  in the Illustris or EAGLE simulations.

One interpretation of this result is that it may be preferable to not fix the slope or use kinematics if the only goal is a minimally biased value of  $h$ . Unbroken degeneracies will increase the scatter of the distribution, but may not bias the recovery as drastically as constraining slope to the incorrect value would. We suggest future studies carefully consider the potential pitfalls of biases inherent to the inclusion of stellar kinematics.

Finally, we were motivated to search for an observable selection criterion which could reduce either the bias or scatter in  $h$ . We cannot confirm the findings of Tagore et al. (2018) that cusp/fold/cross orientations have an effect on the recovery of  $h$ , but we do find noticeable reduction in scatter for quads with images which span a greater range of radii (Fig. 6). When limiting our sample to quads with  $\Delta r/R_E \geq 0.2$ , the scatter is reduced in all cases. We note that this selection introduces substantial bias in the case of Model A, which is the model most different from a power law. This bias merits caution with respect to the utility of this selection in real surveys.

We would like to conclude by saying that lensing degeneracies are a subtle and treacherous reality. Their numerous manifestations are hidden behind high dimensional fitting processes, making them difficult to parse. The reasoning of Xu et al. (2016) appears solid, and yet the prediction does not match reality. Our interpretations regarding stellar kinematic constraints may too be flawed in some deeper way. The way forward must be through the creation of mock systems complete with stellar kinematic models consistent with the methodology of observational studies. A major challenge is that these additional complications introduce even more parameters for degeneracies to lurk within. These degeneracies must be tackled in order to reliably constrain  $H_0$  to the 1% level.

## REFERENCES

- Abbott T. M. C., et al., 2018, *MNRAS*, **480**, 3879
- Barnabè M., Czoske O., Koopmans L. V. E., Treu T., Bolton A. S., 2011, *MNRAS*, **415**, 2215
- Bonvin V., Tewes M., Courbin F., Kuntzer T., Sluse D., Meylan G., 2016, *A&A*, **585**, A88
- Bonvin V., et al., 2017, *MNRAS*, **465**, 4914
- Courbin F., Eigenbrod A., Vuissoz C., Meylan G., Magain P., 2004, *Proceedings of the International Astronomical Union*, 2004, 297a–Å303
- Czoske O., Barnabè M., Koopmans L. V. E., Treu T., Bolton A. S., 2008, *MNRAS*, **384**, 987
- Czoske O., Barnabè M., Koopmans L. V. E., Treu T., Bolton A. S., 2012, *MNRAS*, **419**, 656
- D’Arcy Kenworthy W., Scolnic D., Riess A., 2019, arXiv e-prints, p. arXiv:1901.08681
- Falco E. E., Gorenstein M. V., Shapiro I. I., 1985, *ApJ*, **289**, L1
- Fleury P., Clarkson C., Maartens R., 2017, *Journal of Cosmology and Astroparticle Physics*, 2017, 062
- Freedman W. L., et al., 2019, arXiv e-prints, p. arXiv:1907.05922
- Golse G., Kneib J.-P., 2002, *A&A*, **390**, 821
- Gomer M. R., Williams L. L. R., 2018, *MNRAS*, **475**, 1987
- Keeton C. R., 2001, arXiv e-prints, pp astro-ph/0102340
- Lefor A. T., Futamase T., Akhlaghi M., 2013, *New Astron. Rev.*, **57**, 1
- Meneghetti M., Bartelmann M., Moscardini L., 2003, *MNRAS*, **340**, 105
- Nightingale J. W., Dye S., Massey R. J., 2018, *MNRAS*, **478**, 4738
- Planck Collaboration et al., 2018, arXiv e-prints, p. arXiv:1807.06209
- Power C., Navarro J. F., Jenkins A., Frenk C. S., White S. D. M., Springel V., Stadel J., Quinn T., 2003, *MNRAS*, **338**, 14
- Press A. H., Teukolsky S. A., Vetterling W. T., Flannery B. P., 1992, *Numerical Recipes in C: The Art of Scientific Computing*, 2 edn. Vol. 1, Cambridge University Press, The Pitt Building, Trumpington Street, Cambridge CB2 1RP

- Rathna Kumar S., et al., 2013, *A&A*, **557**, A44  
 Refsdal S., 1964, *MNRAS*, **128**, 307  
 Riess A. G., et al., 2016, *ApJ*, **826**, 56  
 Riess A. G., Casertano S., Yuan W., Macri L. M., Scolnic D., 2019, *ApJ*, **876**, 85  
 Rusu C. E., et al., 2017, *MNRAS*, **467**, 4220  
 Schechter P. L., et al., 1997, *ApJ*, **475**, L85  
 Schneider P., Sluse D., 2013, *A&A*, **559**, A37  
 Sluse D., et al., 2017, *MNRAS*, **470**, 4838  
 Suyu S. H., Marshall P. J., Auger M. W., Hilbert S., Blandford R. D., Koopmans L. V. E., Fassnacht C. D., Treu T., 2010, *ApJ*, **711**, 201  
 Suyu S. H., et al., 2014, *ApJ*, **788**, L35  
 Suyu S. H., et al., 2017, *MNRAS*, **468**, 2590  
 Tagore A. S., Barnes D. J., Jackson N., Kay S. T., Schaller M., Schaye J., Theuns T., 2018, *MNRAS*, **474**, 3403  
 Tewes M., et al., 2013, *A&A*, **556**, A22  
 Wollesenbet A. G., Williams L. L. R., 2012, *MNRAS*, **420**, 2944  
 Wollesenbet A. G., Williams L. L. R., 2015, *MNRAS*, **454**, 862  
 Wong K. C., et al., 2017, *MNRAS*, **465**, 4895  
 Wong K. C., et al., 2019, arXiv e-prints, p. [arXiv:1907.04869](https://arxiv.org/abs/1907.04869)  
 Xu D., Sluse D., Schneider P., Springel V., Vogelsberger M., Nelson D., Hernquist L., 2016, *MNRAS*, **456**, 739  
 van den Bosch F. C., Ogiya G., 2018, *MNRAS*, **475**, 4066

## APPENDIX A: CONSISTENCY CHECKS

As test for robustness, we run a few alterations to our fitting to confirm the resulting distributions of  $h$  are unaffected by our particular fitting process. These alterations are done with respect to Model D test with the slope allowed to vary, with the anticipation that they will apply similarly to all other fittings in this paper. We describe these tests in detail here. We did not perform the MLE determination of  $h$  for these tests, so results should be compared with the blue histogram in Figure 3 for Model D.

The first alteration happens on the very first step of the fitting procedure described in Section 2, where the ellipticity and shear are held at 0.1 to search over the values for position angle and shear angle. This initialization value was set to 0.1 for both shear and ellipticity, which is defined in `lensmodel` as  $1 - q$ . Since this value is an arbitrary choice on our part, we decided to test the effect of increasing it to 0.3, a value more extreme than in any of the lenses. The resulting distribution of  $h$  is not measurably different from the unaltered Model D, with  $h = 0.969_{-0.173}^{+0.040}$ ,  $f_{\chi^2/dof} < 1 = 0.99$ , and  $R_{ell} = 1.00$ . When a KS test is performed to compare the  $h$  distributions, the p-value is 73%.

The second modification is to change the bounds over which the shear/ellipticity grid search is performed in the second run. The unaltered version searches over values between 0.0 and 0.4 for both ellipticity and shear. This test instead searches over more extreme values which are not consistent with zero, from 0.1 to 0.6. Again the goal is to show that even if one makes extreme choices in the fitting setup, the results are robust. Again the resulting distribution of  $h$  is the same as the unaltered Model D, with  $h = 0.975_{-0.218}^{+0.020}$ ,  $f_{\chi^2/dof} < 1 = 0.94$ ,  $R_{ell} = 1.00$ , and a p-value of 67%.

One final test of robustness is performed. This time we are curious not about the fitting initialization parameters, but about whether 100 quads is a sufficient number to accurately determine the distribution of  $h$ . We therefore run one test for Model D which is the same as the unaltered

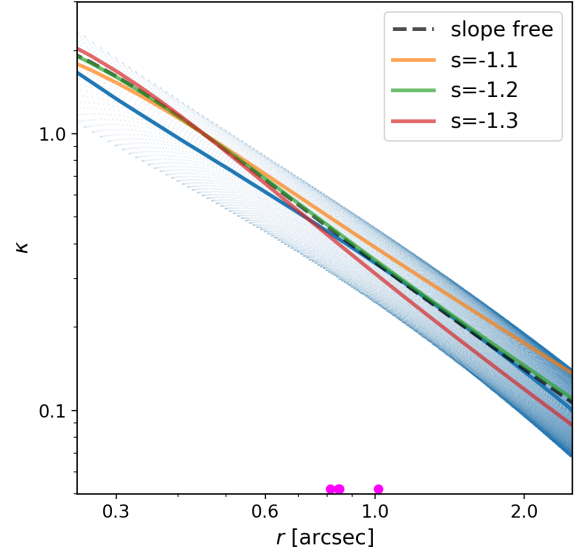


**Figure B1.** Convergence as a function of radius for the Model D input lens (blue) and several power-law fits to the image positions and time delays. Because the lens is elliptical, the density takes on a range of values at any given radius. The circularly averaged profile is depicted by the solid blue line. When the slope is free to vary, the dashed black curve is recovered, while the solid yellow, green, and red curves correspond to the slope being held at -1.1, -1.2, and -1.3, respectively. The magenta points near the horizontal axis depict the radial positions of the images. For comparison with Figure 2, 1 arcsecond corresponds to approximately 6.7 kpc, varying slightly depending on the recovered value of  $h$  for a given model.

test except that it has 500 quads instead of 100. The result is a distribution with  $h = 0.973_{-0.168}^{+0.029}$ ,  $f_{\chi^2/dof} < 1 = 0.95$ ,  $R_{ell} = 1.00$ , p-value of 99%.

The distributions across these tests are indistinguishable. We therefore conclude that our distributions of  $h$  are not significantly affected by either our fitting procedure or by small-number statistics. The main quantity of interest, the median of  $h$ , varies by 0.006 across these tests, which is less than the 1% benchmark to which we desire accuracy.

## APPENDIX B: SINGLE QUAD FITTING

Here we present a thorough analysis of a single quad from Model D, fit with different values of slope. This particular quad returns a nearly unbiased value of  $h$  when the slope is free to vary (0.991 relative to 1.0). For comparison with Figure 6,  $\theta_{23} = 56^\circ$  and  $\Delta r/R_E = 0.24$ . Figure B1 shows the mass density as a function of radius for the synthetic lens as well as several different fits to the image positions and time delays. All fits lie within the scatter of the points, but the fit that matches the true profile best is that when the slope is free to vary. In this case, the recovered slope is  $-1.214$ . When the slope is held, the results are as follows, with the relative bias on  $h$  in parentheses:  $s = -1.1$  (0.902),  $s = -1.2$  (0.986),  $s = -1.3$  (1.005).

Figure B2 compares the time delay surfaces of the true

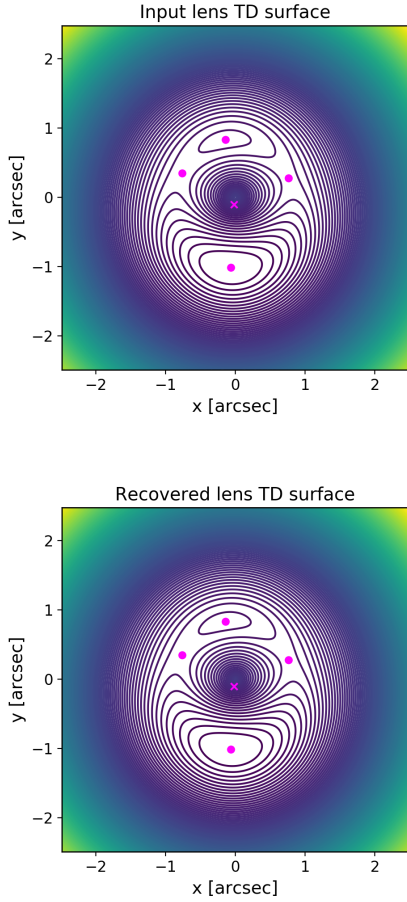


**Figure B2.** Time delay surfaces for the input lens/quad (top) and the recovered model lens/quad for the fit where the slope is allowed to vary (bottom). The image positions (magenta points) are recovered very well and the shape of the time delay surface matches very closely.

input quad (top) and the best-fit result from the case where the slope is free to vary. The surface is reproduced well, with images and time delays matching the quad too accurately to discern by eye ( $\chi^2/dof \simeq 10^{-3}$ ). To explore this, Figure B3 plots the residual difference between the true lensing potential and the fit potential, now as a 1D function of radius, for each of the four fits from Figure B1. Since potentials allow for an arbitrary choice of vertical offset, we choose to set the comparison to equate the first-arriving image. A good match would be represented by the points being laid out in a flat surface with nearly zero residual. Since  $\chi^2$  is calculated with an uncertainty of 0.1 days, as long as the surface residuals are within 0.1 days of zero, the time-delay  $\chi^2$  will be small. The closest match of the four fits is the case where the slope is allowed to vary, which closely matches the time-delay surface between  $r = 0.5''$  and  $r = 1.75''$ . All fits result in the image time delays being less than  $1\sigma$  from the true values, except the case where slope is held at -1.3, which has one image off by  $\simeq 1.2\sigma$ .

The images and time delays of this quad are well-recovered by the fitting procedure, instilling confidence that the results for the large set of quads are reliable.

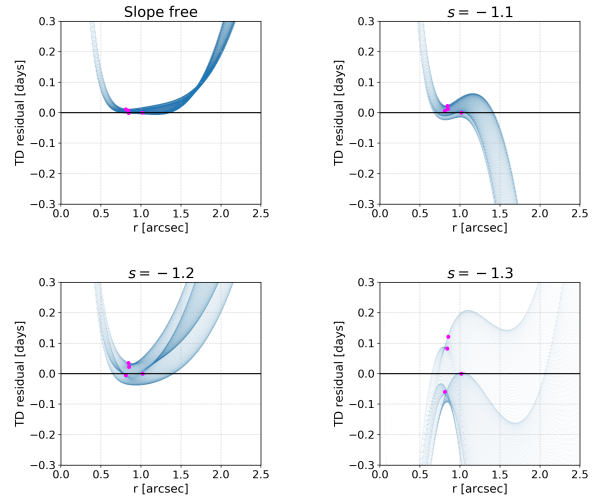


**Figure B3.** Residuals of the fit time delay surface relative to the input lens. In the top left panel, each blue point corresponds to a single pixel of Figure B2, where the slope is free to vary in the fitting procedure. For each pixel, the difference has been evaluated between input surface and the fit surface (top and bottom panels of Fig. B2) and plotted now a 1D function of radius. The image locations themselves are represented as magenta points. The arbitrary offset of lensing potential is set such that the value for the first-arriving image matches across the two models. The fit surface matches the input quad very well, especially for radii between  $0.5''$  and  $1.75''$ , evidenced by the fact that the residual in this region is nearly zero (the time-delay uncertainty in the evaluation of  $\chi^2$  is 0.1 days). The remaining panels show the fits for the three cases where the slope is held at a particular value. As evident by the larger vertical spread in the residuals, these fits do not match the actual surface as well as the case where the slope is free to vary. Nonetheless, the vertical spread of the images is fairly small, confirming that the time delay differences between the images are close to their correct values (within about  $1.2\sigma$  in the worst case, where slope is fixed at -1.3).

This paper has been typeset from a  $\text{\TeX}/\text{\LaTeX}$  file prepared by the author.